Opto-Electronic Advances

ISSN 2096-4579 CN 51-1781/TN

Focus control of wide-angle metalens based on digitally encoded metasurface

Yi Chen, Simeng Zhang, Ying Tian, Chenxia Li, Wenlong Huang, Yixin Liu, Yongxing Jin, Bo Fang, Zhi Hong and Xufeng Jing

Citation: Chen Y, Zhang SM, Tian Y, et al. Focus control of wide-angle metalens based on digitally encoded metasurface. *Opto-Electron Adv* **7**, 240095(2024).

https://doi.org/10.29026/oea.2024.240095

Received: 25 April 2024; Accepted: 1 July 2024; Published online: 23 July 2024

Opto-Electronic Advances

Article

August 2024, Vol. 7, No. 8

DOI: 10.29026/oea.2024.240095

Focus control of wide-angle metalens based on digitally encoded metasurface

Yi Chen[1], Simeng Zhang[1,2], Ying Tian[1]*, Chenxia Li[1], Wenlong Huang[1], Yixin Liu[1,2], Yongxing Jin[1], Bo Fang[3], Zhi Hong[2,4] and Xufeng Jing[2,4]*

Based on the principle of super-symmetric lens with quadratic phase gradient transformation, combined with the principle of digital coding of metasurface, we propose a wide-angle coded metalens for focusing control in two-dimensional space. This metalens achieves focus shift in the *x*-direction by changing the oblique incidence angle of the incident wave, and focus control in the *y*-direction by combining with the convolution principle of the digitally coded metasurface to achieve flexible control of light focusing in the two-dimensional plane. The metasurface unit is mainly composed of three-layer of metal structure and two layers of medium, and the transmission phase is obtained by changing the middle layer of metal structure, which in turn obtains the required phase distribution of the metalens. The design of the metalens realizes the function of the lens with a large viewing angle at the *x*-polarized incidence, and realizes two-dimensional focus control. Experimentally, we prepared the designed coding metalens and tested the focus control function of the wide-angle coding metalens. The experimental results are in good agreement with the design results.

Keywords: metasurface; metalens; wide-angle; coding

Chen Y, Zhang SM, Tian Y et al. Focus control of wide-angle metalens based on digitally encoded metasurface. *Opto-Electron Adv* **7**, 240095 (2024).

Introduction

Metasurface is a two-dimensional artificial electromagnetic material composed of sub-wavelength unit structures in a specific arrangement, which is used to control the propagation of electromagnetic waves[1]. With its ultra-thin structure and unique working principle, it avoids the disadvantages of large size, complex structure, and difficulty in integration caused by traditional optical devices. By designing the phase, amplitude, polarization state of the sub-wavelength unit structure, a metasurface that is small in size, easy to integrate, and highly convenient can be obtained[2]. Through complex designs of different unit structures, metasurfaces can achieve physical effects that are difficult to produce in nature, such as negative refraction[3,4], polarization rotation[5–7], zero refractive index[8,9], convergence imaging[10], and complex beams[11–13]. These physical effects can be used to design and produce optical devices with various new functions, such as holographic projection[14,15], radar stealth[16], absorbers[17], deflectors[18], beam splitters[19], metalenses[20], biosensors[21–23] and other optical functional devices[24–32].

In recent years, the research on metalens[33] has been greatly developed. These metalens utilize the small size, ultrathinness and ability of metasurfaces to manipulate incident wave to achieve a focusing effect[34]. They have an

[1]Institute of Optoelectronic Technology, China Jiliang University, Hangzhou 310018, China; [2]Centre for THz Research, China Jiliang University, Hangzhou 310018, China; [3]College of Metrology & Measurement Engineering, China Jiliang University, Hangzhou 310018, China; [4]College of Information Engineering, China Jiliang University, Hangzhou 310018, China.

*Correspondence: Y Tian, E-mail: tianyingcjlu@163.com; XF Jing, E-mail: jingxufeng@cjlu.edu.cn

Received: 25 April 2024; Accepted: 1 July 2024; Published online: 23 July 2024

irreplaceable role in the development of planar optical devices[35–37]. Currently, metalenses are applied in various wavelength bands such as visible, mid-infrared, and terahertz. For example, Ramon et al.[38] have implemented a high numerical aperture metalens based on all-dielectric unit structure in the visible light band. Wang et al.[39] used the geometric phase to obtain a metalens with achromatic focusing in the near-infrared wavelength band. Gao et al.[40] designed a polarization-insensitive silicon-based metalens in the terahertz band. However, most current metalens are only suitable for the normally incidence on the metasurface to produce a focusing effect. When light is incident on the metasurface obliquely, the focusing effect of the metasurface will be greatly weakened, or even unable to produce a focusing effect. In order to make the metasurface achieve the focusing function in a wider range of incident angle, Pu et al.[41–46] proposed a supersymmetric lens by investigating the properties of Luneburg lenses and compound eyes to realize a wide-angle planar lens based on a fast phase gradient. However, this lens is unable to realize the free regulation of focus.

Therefore, we used the principle of supersymmetric lenses and combined with the principle of metasurface digital coding to design a wide-angle metalens[47], which can achieve flexible control of the focus in two-dimensional space. The unit structure of the wide-angle lens is composed of three layers of metal and two layers of media. By changing the size of the unit structure, the transmission phase required to satisfy the coding of the wide-angle metalens is obtained. By changing the incident angle in the x-axis direction, the focus is flexibly achieved on the x-axis. On the y-axis direction, we used the coding convolution principle to achieve focus control in this direction. We further propose to utilize the principle of coded addition to achieve multifocus effect. We designed the digitally encoded wide-angle metalens through simulation, and finally verified through experiments, proving the two-dimensional control of the digitally encoded wide-angle metalens on the focal plane.

Principles and Design

Design principles of metalenses

The traditional lens design is based on the different optical path differences caused by the different thicknesses of light passing through different positions of the lens, which causes the transmitted light to focus. However, the emergence of metasurfaces provides new design ideas for lens. The sub-wavelength structure of the metasurface causes the phase mutation after the light is incident, which leads to a new light propagation law called the generalized Snell's law[48]. According to the law, we can get the phase distribution of each position on metalens as

$$\varphi(r) = \frac{2\pi}{\lambda}\left(\sqrt{r^2+f^2}-f\right), \tag{1}$$

where λ is the operating wavelength, r is the radial distance from the centre of the lens, and f is the focal length corresponding to the metalens. Divide the metalens into each small unit, and use the above Eq. (1) to discretize the phase of the entire lens to obtain the phase corresponding to each unit. In this way, we can obtain a metalens that is thinner, lighter, and easier to integrate.

Recently, Pu et al.[41] proposed a metalens with a quadratic phase distribution function, called a supersymmetric lens, which has good wide-angle lens performance. Its phase distribution function follows a quadratic distribution as

$$\varphi(r) = k_0\frac{r^2}{2f}, \tag{2}$$

where k_0 is the number of waves in free space, and both f and r represent the same meaning as Eq. (1), which denote the focal length of the metalens and the radial distance from the centre of the lens, respectively. It can be seen by Eq. (2) that the formula represents the phase distribution function of light incident along the normal direction. Therefore, when the light wave is incident obliquely on the metalens, assuming that the incident wave is located on the xz plane and the angle with the normal direction is θ, the phase carried by the transmitted light is shown as[41]

$$\begin{aligned}\varphi(r) =& k_0\frac{r^2}{2f} + k_0 x\sin\theta \\ =& \frac{k_0}{2f}\left((x+f\sin\theta)^2+y^2\right) - \frac{fk_0\sin^2\theta}{2},\end{aligned} \tag{3}$$

In contrast to Eq. (2), $k_0 x\sin\theta$ in Eq. (3) is the phase change caused by the oblique incidence of light. Observe that the last term of the right-hand side of the Eq. (3) is independent of r and can be neglected, so that when light is incident obliquely on the metalens, the focus can be well focused on the same focal plane and only shifted transversely in the x-direction of the focal plane by the amount of $f\sin\theta$.

The wide-angle metalens design

In order to achieve the wide-angle metalens performance, we designed a unit structure consisting of three

layers of metal, the upper and lower layers of the unit structure consist of two parallel metal grating strips, and the upper and lower layers of the grating strips are perpendicularly distributed, and the middle layer consists of the notched ring and the metal rod with diagonal symmetry axes. Each metal layer is separated by a dielectric layer. The schematic diagram is shown in Fig. 1. The unit structure period is p=4 mm. All metal layers are made of conductive copper. The conductivity is σ =5.8×10^7 S/m and the thickness is 0.035 mm. The upper and lower grating bars are polarization-selected grating with a width of L_1=0.8 mm and a mutual spacing of L_2=0.7 mm. The width of the middle layer ring and the metal rod is w=0.38 mm, the radius of the ring is r=1.9 mm. The initial values of angles α and β are 60° and 45°, respectively. The grating strip combined with the open ring of the middle layer makes the electromagnetic wave repeatedly reflected and transmitted inside the unit, and improves the cross-polarization efficiency of the unit structure. Considering the simulation effect and processing cost, FR4 was chosen as the base of the unit structure, with a relative dielectric constant of 4.3 and a thickness of d_0=1.6 mm. Through simulation, we can observe that at 8 GHz, when the incident wave is incident with x-polarization, the cross-polarized transmitted light achieves good transmission efficiency, and the other scattering modes are in a low condition at this operating frequency as shown in Fig. 2(a).

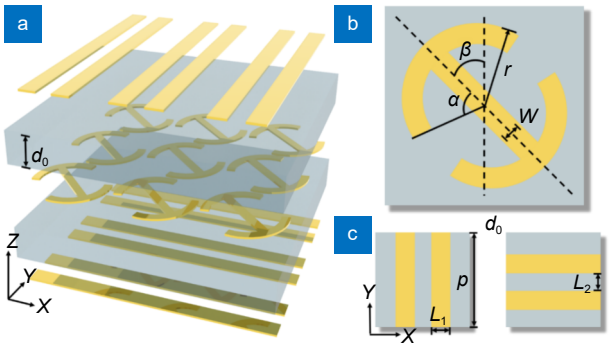

Fig. 1 | Schematic diagram of metalens unit.

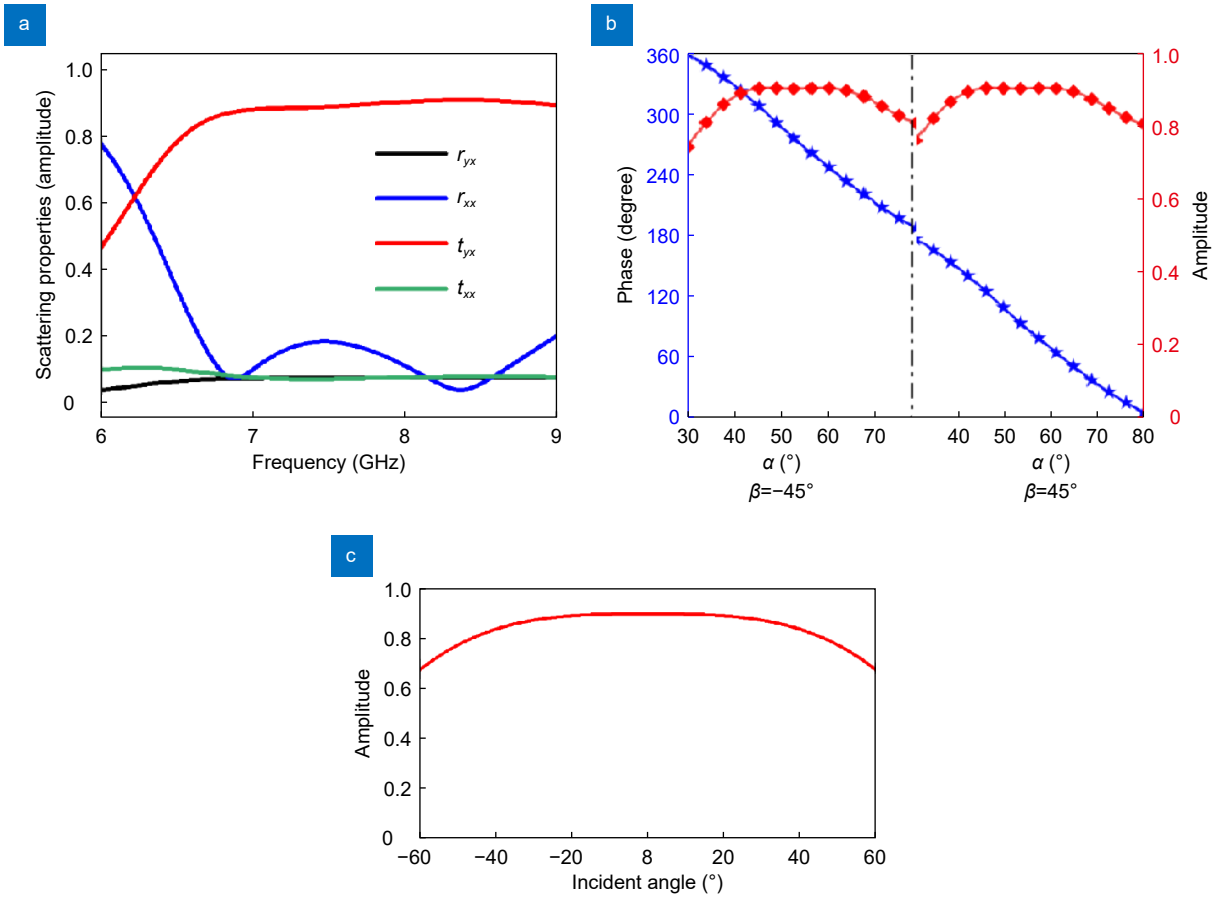

Fig. 2 | (**a**) Scattering characteristics of the unit structure in the range of 6 to 9 GHz. (**b**) Curves of the phase and transmission amplitude of the unit with respect to the interlayer circular angle α and symmetry direction β at 8 GHz. (**c**) Transmission amplitude diagram of the unit structure in the range of −60° to 60°.

To achieve a good metalens function, in addition to having good transmission efficiency, the unit also needs to meet the corresponding phase changes. By changing the angles α and β of the middle layer ring of the unit structure, we can obtain any phase change between 0 and 2π, as shown in Fig. 2(b). When β=45°, changing the angle α in the range of 30°–80°, the unit structure can cover the phase of 0–180°. When β=−45°, changing the angle α in the range of 30°–80°, and the unit structure can cover the phase of 180°–360°. At the same time, it can be observed from Fig. 2(b) that most of the transmission amplitudes of the unit structure are above 0.8. When the light is oblique incident into the element structure, the transmission amplitude of the cross polarization is shown in Fig. 2(c).

Based on the design principle of the wide-angle metalens, we discretise the phase at each spatial position of the metalens, and the phase values at each point can be introduced by Eq. (2). By changing the unit structure parameters α and β, the optimal design operation is carried out to obtain the required transmission phases of the unit structure at different positions. The unit structures that meet the requirements are arranged in an orderly manner according to a certain phase gradient law to obtain a metasurface with wide-angle metalens performance, and the focusing schematic of this meatsurface is shown in Fig. 3. When the plane wave is incident on the metalens at different oblique angles of incidence, the transmitted light is focused on the same focal plane and produces only a transverse positional shift.

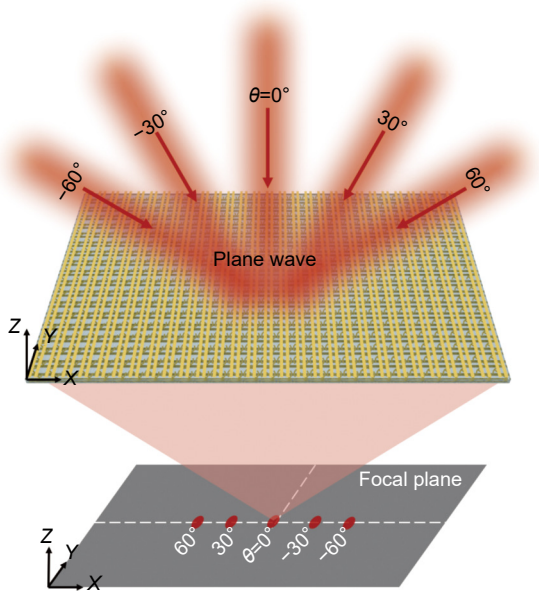

Fig. 3 | Schematic diagram of wide-angle metalens focusing.

In order to compare the focusing effects of traditional metalens and wide-angle metalens, two types of metalens were designed using the above unit structure. The phase distribution function of the traditional metalens is shown in Eq. (1), and its phase change is related to the diameter from the center of the lens. It changes linearly with the distance, and the phase distribution of the wide-angle metalens is shown in Eq. (2). Through simulation using the finite-difference time-domain method, using the CST MICROWAVE STUDIO software, the *x*-polarized wave is used as the incident wave. The corresponding metasurface is simulated, and the near-field monitor is placed to obtain the electric field intensity distribution of the outgoing light. We obtained the simulation results as shown in Fig. 4. Figure 4 shows the electric field distribution between a linear phase distribution metalens and a quadratic phase gradient wide-angle metalens under the same incident conditions. Figure 4(a) shows the electric field intensity diagram at each incident angle with linear phase distribution. It can be observed that when the incident wave is normal, the metalens has a good focusing effect, and when the incident wave is obliquely incident on the metalens, with the increase of the angle, the focal light intensity decreases rapidly and cannot be focussed to the same focal plane. Comparing the observation with Fig. 4(b), it can be seen that unlike the metalens with linear phase distribution, when light is obliquely incident on the wide-angle lens with quadratic phase distribution, the focus is almost in the same focal plane, and only produces a certain offset in the lateral direction.

Design of wide angle coding metalenses

The wide-angle metalens in the above section only realize the regulation of the focus in the *x* direction. In order to achieve the regulation of the focus in two-dimensional space, based on the design basis of the wide-angle metalens, we further designed the lens in the *y* direction and incorporated the principle of digitally coded metasurfaces for electromagnetic wave control. Combined with the digital coding metasurface function, the units satisfying the coding function are designed, and the units are combined in various ways to realize the deflection of the focus. This design is based on a coding principle of scattering mode offset proposed by Fourier transform, which is called the convolution theorem[49]. It expresses the transformation relationship between the signal in the time domain and the frequency domain, as shown in Eq. (4),

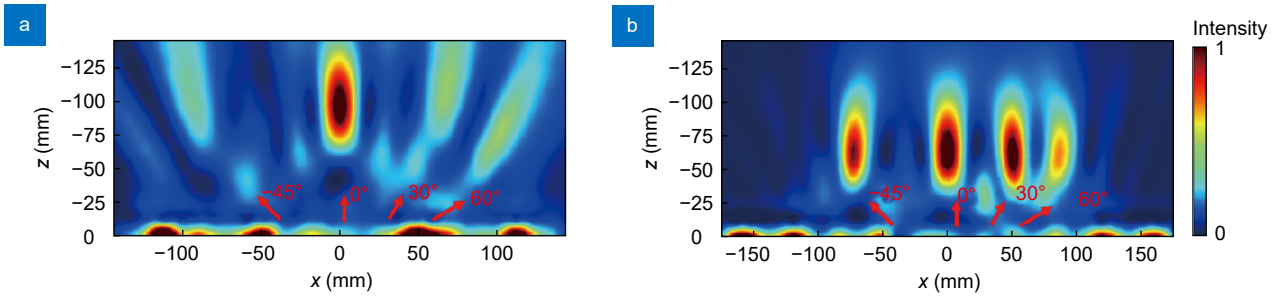

Fig. 4 | Normalized electric field intensity distribution of the metalens in the *x*-*z* plane for θ = −45°, θ = 0°, θ = 30°, θ = 60° at an operating frequency of 8 GHz. (**a**) Shows the electric field intensity distribution of the metalens with linear phase distribution. (**b**) Shows the electric field intensity distribution of the wide-angle metalens with quadratic phase distribution.

$$f(t)\cdot g(t)\overset{FFT}{\Leftrightarrow}f(\omega)*g(\omega)\ . \tag{4}$$

Transforming $g(\omega)$ in Eq. (4) into a Dirac-delta function, it can be obtained as

$$f(t)\cdot\exp(\mathrm{j}\omega_0 t)\overset{FFT}{\Leftrightarrow}f(\omega)*\delta(\omega-\omega_0)=f(\omega-\omega_0)\ , \tag{5}$$

where $\exp(\mathrm{j}\omega_0 t)$ is the time-shift term in the time domain. Eq. (5) shows that the convolution operation between the spectrum and the impulse function produces only an offset of ω_0 in the spectrum but no distortion. For the coded metasurface, the Fourier transform pair is satisfied between its near field distribution and far-field scattering. Professor Cui research group introduced convolution operation into the design of coded patterns, and used Fourier transform in digital information theory to design and manipulate coded patterns[49]. Therefore, after replacing the independent variables t and ω in Eq. (4) with x_λ and $\sin\theta$, the scattering pattern offset function can be obtained as

$$\begin{aligned}f(x_\lambda)\cdot\exp(\mathrm{j}x_\lambda\sin\theta_0)&\overset{FFT}{\Leftrightarrow}E(\sin\theta)*\delta(\sin\theta-\sin\theta_0)\\&=E(\sin\theta-\sin\theta_0)\ ,\end{aligned} \tag{6}$$

where $x_\lambda = x/\lambda$, θ is the incident angle of the wave with respect to the normal direction, and $\exp(\mathrm{j}x_\lambda\sin\theta_0)$ describes the gradient phase with respect to a given direction. As can be seen in Eq. (6), the $f(x_\lambda)$ of the metasurface in the coding mode can be regarded as one of the time domain signals in the Fourier transform process, the gradient coding sequence $\exp(\mathrm{j}x_\lambda\sin\theta_0)$ is the other time domain signal, and the radiation direction pattern determined by the original coding pattern is expressed as $E(\sin\theta)$. The frequency domain signal $E(\sin\theta-\sin\theta_0)$ is obtained after the Fourier transform is performed by multiplying $f(x_\lambda)$ with $\exp(\mathrm{j}x_\lambda\sin\theta_0)$. It can be observed that the far-field scattering pattern is shifted to another direction, becoming $E(\sin\theta-\sin\theta_0)$. The product of $f(x_\lambda)$ in the coded mode and the gradient coding sequence $\exp(\mathrm{j}x_\lambda\sin\theta_0)$ leads to the deflection of the far-field scattering from the coded metasurface in a predetermined direction.

Therefore, by using the wide-angle metalens designed previously combined with the design principle of coded metasurface convolution, the wide-angle metalens can be flexibly controlled in the y direction. The unit structure is consistent with the above structure. Based on the unit group satisfying the quadratic phase distribution in the x direction, further parameter optimization is carried out to obtain the unit group satisfying the phase difference between adjacent units of 45° in the y direction, that is, the 3-bit coding is satisfied in the y direction. Through simulation, the unit structure parameters that meet the 3-bit encoding phase distribution characteristics are obtained. The scattering amplitude and phase distribution of a group of coding units are shown in Fig. 5. It can be seen from Fig. 5(a) that the transmission amplitude of the coding unit has reached 0.8. Figure 5(b) demonstrates the phase distribution of the coding unit. It can be observed that the phase difference between each coding unit is roughly maintained at about 45°, which satisfies phase distribution characteristics between 3-bit coding units. At this time, the metasurface can realize wide-angle focusing in the x direction, and has the property of encoding metasurface in the y direction, and can perform coded convolution and addition operations, so as to realize focus regulation and multi-focus independent control in two-dimensional space.

In order to prove the reliability of the design of the wide-angle metalens combined with the coded metasurface principle, we conducted simulations of metalens with different coding sequence arrangements in the y-direction of the lens. First, give a coding sequence S0 (765544333222111100000000111122233344567) in the y direction, so that the metasurface also has a central

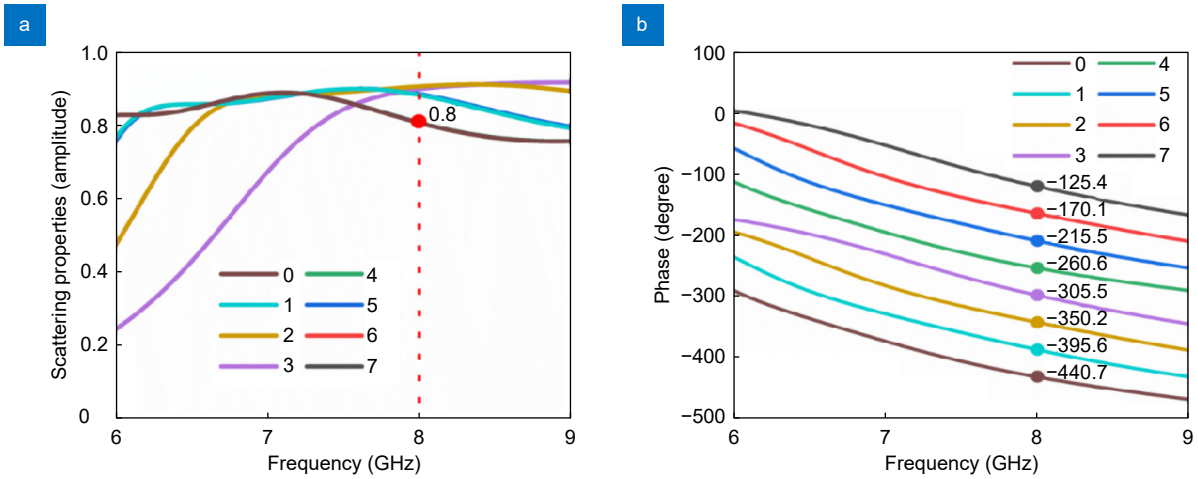

Fig. 5 | Transmission amplitude plot (**a**) and phase distribution (**b**) of the coding unit in the 6-9 GHz range.

aggregation effect in the y direction. Secondly, we designed four groups of basic coding sequences as "0246..." with different period. It is known that the period of the unit structure is of p, then the periods of the four sets of coding sequences are respectively designed as T_{s1}=12p, T_{s2}=16p, T_{s3}=32p, T_{s4}=40p. The coding pattern of each coding sequence and the coding pattern after the convolution operation are as shown in Fig.6. Figure 6 shows the schematic diagram of the metasurface encoding sequence in the y direction and the schematic diagram of the convolution operation process. Based on the generalized Snell's law, the deflection angle of each coded metasurface scattering mode can be calculated. The deflection angle θ can be calculated as

$$\theta = \sin^{-1}(\lambda / T) \,, \tag{7}$$

where λ is the working wavelength of the metasurface, and T is the period size of the coding sequence. Substituting the periods of the above four sets of coding sequences into the Eq.(7), the theoretical deflection angles of each coding sequence are calculated to be 51.4°, 35.9°, 17°, and 13.6°. After convolving the four sets of coding sequences with the coding sequence S0, the obtained new coding sequences are used to arrange the metasurface array, which can achieve the effect of focusing deflection in the y direction. The metasurface is simulated through the finite difference time domain method, and the focusing effect shown in Fig. 7 is obtained. Observing Fig. 7, we can see that after the plane wave is incident on the metalens, the transmitted light produces the focusing effect on the focal plane (x-y plane). As the coding sequence period continues to increase, the angle at which the focus shifts toward the positive direction of the y-axis becomes smaller and smaller. Observing the light intensity distribution on the y-z plane, the focus deflects in the expected direction. The simulation effect is shown in Fig. 7(ii) . The focal deflection angles of the four groups of coded metalens are 51°, 38°, 18°, and 14°, respectively, and the simulation values are basically consistent with the theoretical values. However, the basic coding sequence mentioned above only simply expands the period by integer multiples, and the deflection angle that can be controlled is limited. In order to control the beam deflection more flexibly, we can flexibly use the convolution theorem to convolve the two basic coding sequences to obtain a hybrid coding sequence, and then perform a convolution operation with the coding sequence S0 to obtain more different focus on the deflection effect. Figure 8(a) shows the focus deflection effect of the hybrid coding sequence S5 after the convolution operation of the basic periodic sequences S3 and S4, and then convolved with the coding sequence S0. Observing Figure 8(a-ii), it can be seen that the hybrid coding sequence S5 obtains a larger angle of focus shift than the basic sequence before mixing, with a deflection angle of 34°. Figure 8(b) shows the hybrid coding sequence S6 after the convolution of the basic coding sequence S3 and the reverse basic coding sequence S1, and the focus deflection effect produced by combining the coding sequence S0. The focus produces a deflection angle of –31°. It can be seen from the simulation that the scattering angle of the mixed encoding sequence is not the direct addition and subtraction of the scattering angles of the basic sequence. According to Eq. (6), we can deduce that the scattering angle of the mixed coding sequence can be calculated as

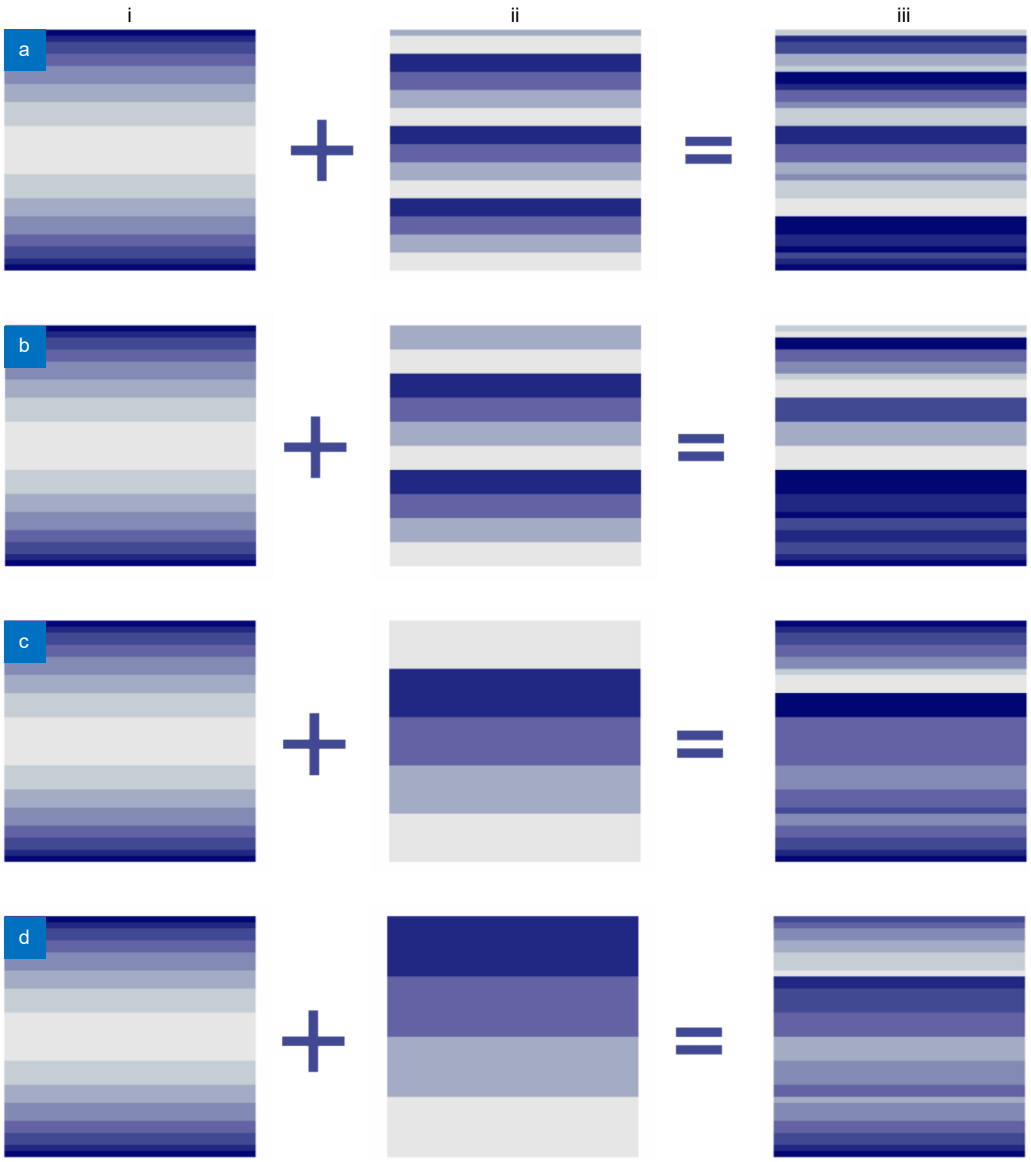

Fig. 6 | Coding patterns of each coding sequence (**a**–**d**) are the coding patterns of coding sequence S0 after convolution operation with coding sequences S1 (T_{S1}=12p), S2 (T_{S2}=16p), S3 (T_{S3}=32p), and S4 (T_{S4}=40p), respectively. i) is the coding sequence S0, ii) from top to bottom are S1, S2, S3, S4, iii) the coding sequence after convolution.

$$\theta = \sin^{-1}(\sin\theta_1 \pm \sin\theta_2)\ , \tag{8}$$

where θ_1 and θ_2 are the deflection angles of the two basic coding periodic sequences for the convolution operation. Through Eq. (8), the theoretical deflection angles of hybrid codes S5 and S6 can be calculated to be 31.8° and −29.2°, respectively. Compared with the theoretical calculation value, the simulation value obtained by the simulation effect basically does not have a large deviation, which proves that the simulation is basically consistent with the theory.

Theoretically, the above-mentioned coding metasurface retains the function of a wide-angle metalens while increasing the control function of the focus in the y direction. While the metasurface satisfies the coding phase distribution in the y direction, the phase in the x direction still maintains the phase distribution characteristics. When the incident wave is located on the x-z plane and is incident obliquely on the metalens, the transmitted light is still focused on the same focal plane and is only laterally shifted in the x direction of the focal plane. In order to prove that the wide-angle metalens performance and the y-direction coding control function exist at the same time, we conducted the simulation again, and the simulation results are shown in Fig.9. We verified the focusing effect of the metalens under 30° oblique incidence. Observing Fig. 9, we can see that under oblique

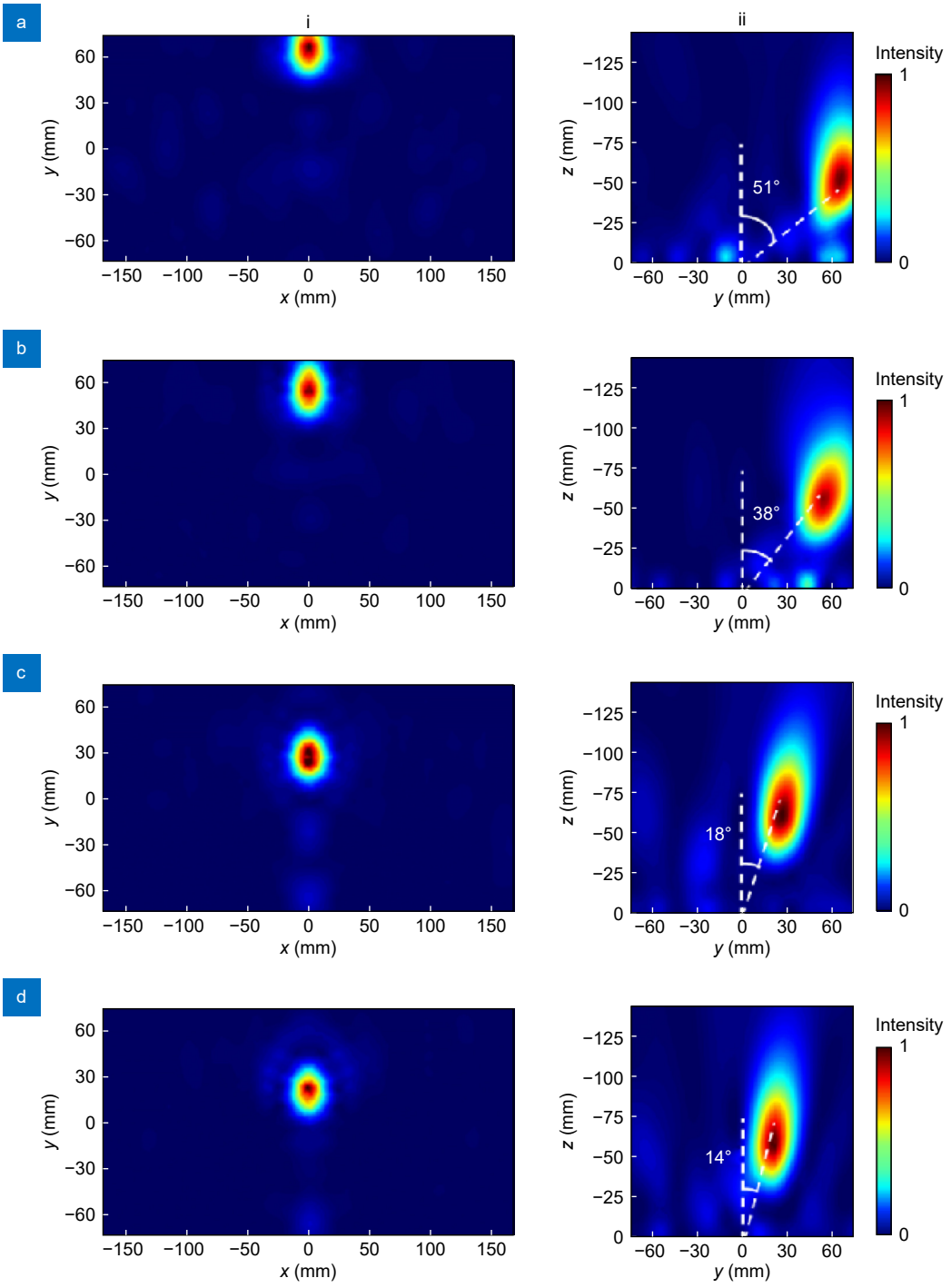

Fig. 7 | In the operating frequency of 8 GHz, the normalized electric field intensity distribution on the *x*-*y* plane and the *y*-*z* plane of the plane wave normal incidence metalens. (**a**) S0 and S1 are convolved to produce a 51° deflection in the *y* direction. (**b**) S0 and S2 are convoluted, a deflection of 38° is produced in the *y* direction. (**c**) After convolution of S0 and S3, a deflection of 18° is produced in the *y* direction. (**d**) After convolution of S0 and S4, a deflection of 14° is produced in the *y* direction.

incidence, the light intensity distribution in the *y*-*z* plane is almost consistent with the light intensity distribution under normal incidence. The deflection effect in the *y* direction is not affected by the tilt angle of the incident wave. At the same time, the focus also produces a shift effect in the *x* direction. Therefore, through simulation, we verified that the metalens can meet the two-dimensional flexible control of its focus in the *x* and *y* directions.

Based on the coding metasurface design principle, we can also extend the coding space to the complex domain

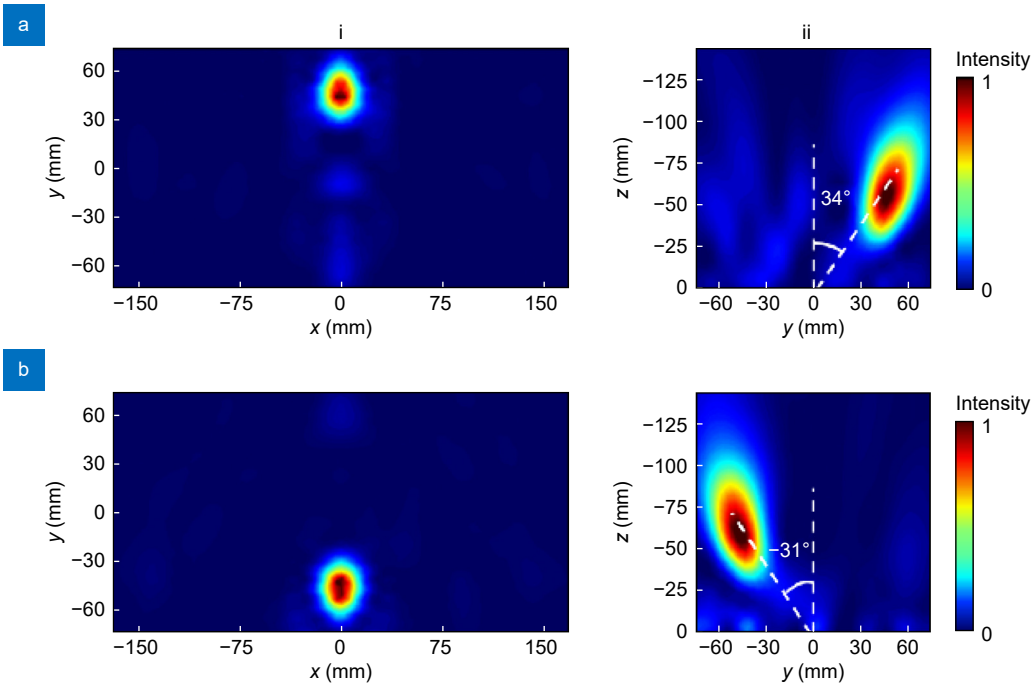

Fig. 8 | In the mixed encoding mode, the normalized electric field intensity distribution of the metalens on the *x*-*y* plane and the *y*-*z* plane. (**a**) After the coding sequences S3 and S4 are mixed, the focus of the metalens is deflected by 34° along the *y*-axis direction. (**b**) After the encoding sequence S3 and the reverse encoding sequence S1 are mixed, the focus of the metalens is deflected by −31° along the *y*-axis direction.

and use the complex coding addition theorem to control electromagnetic waves[49], to achieve the focus function of double focus or even more focus, the deflection angle of each focus can also be designed separately. When the electromagnetic wave is along the positive direction of the z-axis, it can be expressed as

$$\dot{\boldsymbol{E}} = \boldsymbol{E}_0 \mathrm{e}^{-\mathrm{j}kz+\mathrm{j}\varphi} = \boldsymbol{E}_0 \mathrm{e}^{-\mathrm{j}kz}\mathrm{e}^{\mathrm{j}\varphi}\ , \tag{9}$$

where k is the propagation constant, $\mathrm{e}^{\mathrm{j}\varphi}$ contains the phase details of the electromagnetic wave. By controlling the phase of the electromagnetic wave, the scattered beam can be flexibly controlled. Therefore, the addition theorem is a special encoding form based on analytic geometry and complex variable functions. The phase part $\mathrm{e}^{\mathrm{j}\varphi}$ is used for complex encoding, so that there is a certain connection between different bit number codings. The operation rules of the complex encoding addition theorem are shown in Table 1[49] , this rule can be used to calculate the expansion from low bit number to high bit number, thereby realizing more special functions.

Next, we continue to study wide-angle coded metalens using the coded addition theorem. From the above simulation results, it can be seen that the convolution theorem can only independently control the focus of the metalens, and by using the complex addition theorem, we can achieve simultaneous control of the two functions. After the addition operation of the 2-bit coding sequence S7 (0123) with a period of 16p and the 2-bit coding sequence S8 (0123) with a period of 32*p*, a 3-bit mixed coding sequence S9 is obtained. We can convolve the hybrid code S9 with the coding sequence S0 to obtain a new sequence of metasurface arrays as shown in Fig. 10(a). It can be observed that the coded metasurface after addition operation generates two independent focus on the same plane. Through the normalized electric field intensity distribution of the *y*-*z* section, it can be observed that the offsets of the two focuses are 18° and 38°, respectively, which are almost consistent with the offsets produced by the coding sequence before the addition operation. During the addition operation, the two focuses did not interfere with each other. The coding sequences S7 and S8 are used to perform coding addition operations along the opposite coding direction, and simulation is performed to obtain the focusing effect in Fig. 10(b). In Fig. 10(b), the two foci converge in different directions of the *y*-axis, and the offsets remain unchanged as 18° and 38°, respectively. Therefore, through the addition theorem, we further obtain a multi-focus wide-angle encoding metalens, which can achieve multi-focus convergence while arbitrarily controlling the position of the focus in a two-dimensional plane.

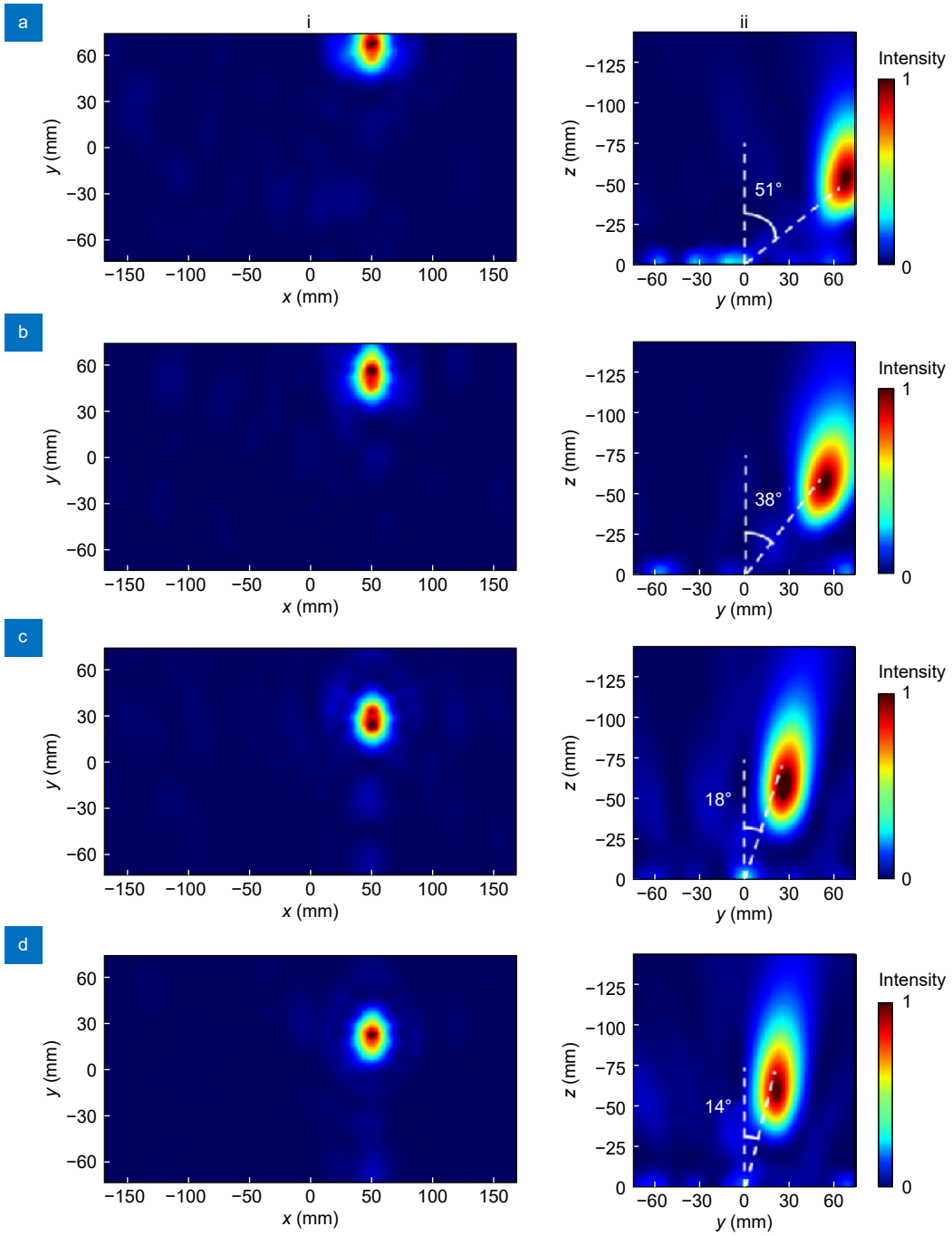

Fig. 9 | In the operating frequency of 8 GHz, when the light wave is obliquely incident on the metalens, the normalized electric field intensity distribution on the *x*-*y* plane and the *y*-*z* plane. (**a**–**d**) are the convolution of the coding sequence S0 with S1, S2, S3 and S4 in the *y* direction respectively, the light wave is incident obliquely on the metalens at an angle of 30°, resulting in a normalized electric field intensity distribution of focus shift. From the column (i), it is observed that the focus shifts in the *x* and *y* directions simultaneously. From the column (ii), it is observed that the oblique incidence of the incident wave to the metalens does not change the deflection angle in the *y* direction, but the focus is offset in the *y* direction, it is also given an offset in the *x*-direction, realizing flexible control of the focus in two-dimensional plane.

Experimental and measurement results

In order to verify the focusing effect of the metalens, we used standard printed circuit board (PCB) technology to produce a sample of the metalens for experimental verification of the focusing function[50–68]. Figure 11 shows the samples of the middle layer structure of the metalens under different functions. The actual size of the metalens sample is of 400×200 mm^2, and the area occupied by the central structure is consistent with the simulation model

Table 1 | operation rules for complex encoding addition from 1-bit to 2-bit, 2-bit to 3-bit.

1 bit→2 bit	2 bit→3 bit
$\dot{0}_1+\dot{0}_1=\dot{0}_2$	$\dot{0}_2+\dot{0}_2=\dot{0}_3\ \dot{1}_2+\dot{0}_2=\dot{1}_3\ \dot{2}_2+\dot{0}_2=\dot{6}_3\ \dot{3}_2+\dot{0}_2=\dot{7}_3$
$\dot{0}_1+\dot{1}_1=\dot{1}_2$	$\dot{0}_2+\dot{1}_2=\dot{1}_3\ \dot{1}_2+\dot{1}_2=\dot{2}_3\ \dot{2}_2+\dot{1}_2=\dot{3}_3\ \dot{3}_2+\dot{1}_2=\dot{0}_3$
$\dot{1}_1+\dot{0}_1=\dot{3}_2$	$\dot{0}_2+\dot{2}_2=\dot{2}_3\ \dot{1}_2+\dot{2}_2=\dot{3}_3\ \dot{2}_2+\dot{2}_2=\dot{4}_3\ \dot{3}_2+\dot{2}_2=\dot{5}_3$
$\dot{1}_1+\dot{1}_1=\dot{2}_2$	$\dot{0}_2+\dot{3}_2=\dot{7}_3\ \dot{1}_2+\dot{3}_2=\dot{4}_3\ \dot{2}_2+\dot{3}_2=\dot{5}_3\ \dot{3}_2+\dot{3}_2=\dot{6}_3$

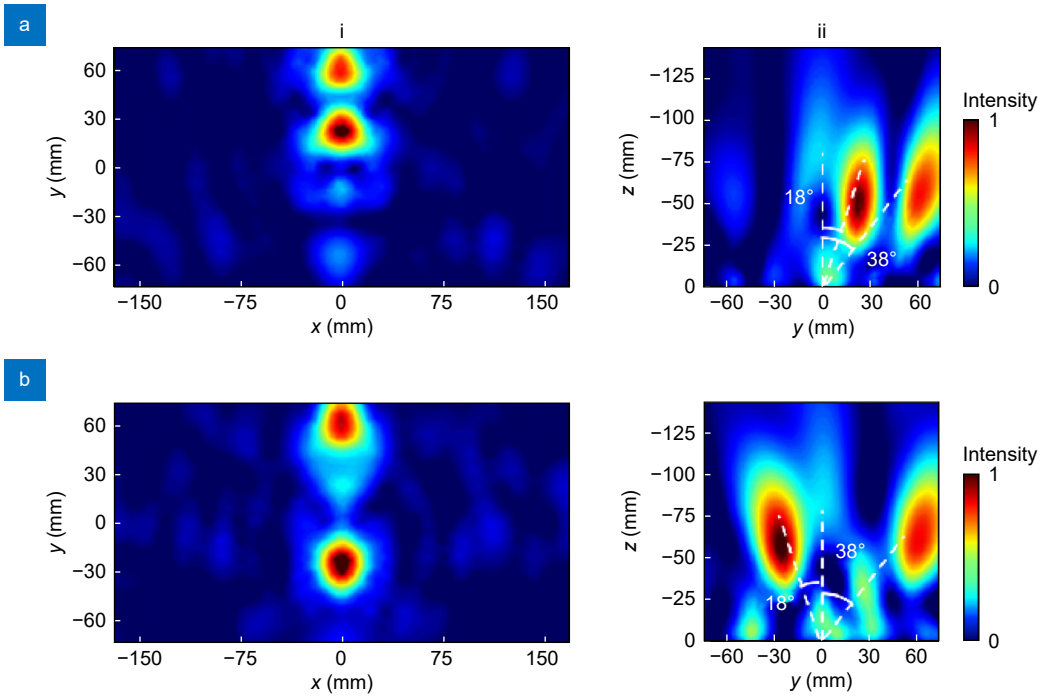

Fig. 10 | Normalized electric field intensity distribution of the coded metalens based on the addition theorem. (**a**) is the normalized electric field distribution of the *x*-*y* section and the *y*-*z* section after the addition of the 2-bit coding sequence S7 (0123) with a period of 16p and the 2-bit coding sequence S8 (0123) with a period of 32*p*. The offset angles of the two focuses are of 18° and 38°, respectively. (**b**) is the normalized electric field distribution of the *x*-*y* cross-section and the *y*-*z* cross-section after the reverse addition operation of the 2-bit coding sequence S7 (0123) with a period of 16*p* and the 2-bit coding sequence S8 (0123) with a period of 32*p*.

with an area of 360×160 mm^2. In order to better fix the metasurface during the test process, the actual size of the metasurface sample is epitaxial by 20 mm on all sides, and screw holes are left for subsequent fixation on the metasurface test frame.

This experiment uses microwave near-field testing system to test the functionality of metasurface samples. The horn antenna is used to connect the vector network analyzer as the transmitting end, and the waveguide detector is used as the signal receiving end to transmit the data back to the vector network analyzer. The vector network analyzer used in the laboratory is Agilent E5071C, which can transmit and receive electromagnetic waves in the frequency range of 100 kHz–8.5 GHz. The horn antenna can transmit signals in the range of 5.38 GHz–8.17 GHz, and the waveguide detector can receive signals in the same frequency band. The test frame is composed of an aluminum alloy metal frame and a stepper motor to achieve controllable movement in three-dimensional space. The stepper motor is connected to the computer through the HF020 controller to realize automatic control of program coding. By modifying the control program in the matlab software, the controller sends out the expected pulse signal, and the stepper motor further receives the signal and turns the signal into the displacement of the platform test frame, thereby controlling the waveguide probe to move in three-dimensional space for data reception. Figure 12 shows the test platform. After connecting to the signal line, the horn antenna sends out a spherical wave, and after a certain distance of

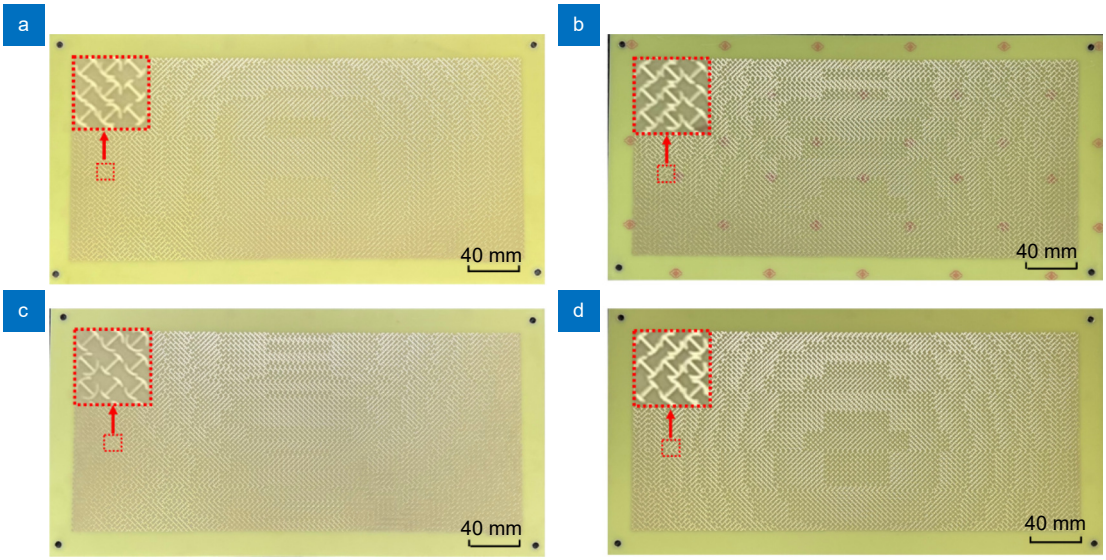

Fig. 11 | Physical picture of the middle structural layer of the metalens sample. (**a**) The metasurface obtained by convolving S0 (focused coding sequence) and S3 (coding sequence with the period of 32*p*). (**b**) The metasurface obtained by convolving S0 (focused coding sequence) and S2 (coding sequence with period 16*p*). (**c**) The metasurface after mixed coding of the coding sequence S3 and the reverse coding sequence S1. (**d**) The metasurface obtained using the addition principle of digitally encoded metasurfaces.

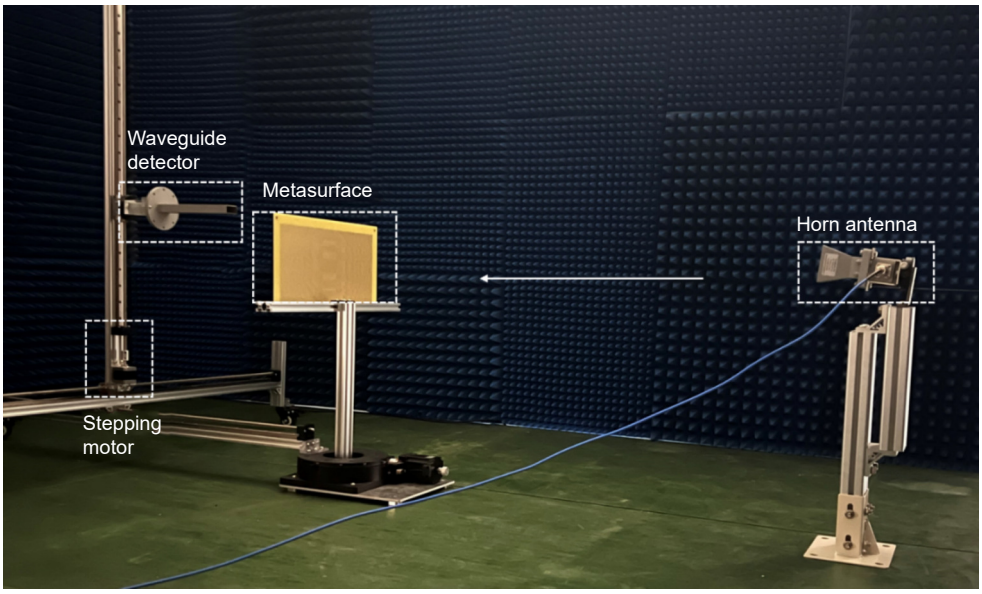

Fig. 12 | Experimental testing platform.

transmission, the spherical wave is slowly transformed into a plane wave. In order to meet the incidence of the antenna as a plane wave to the metasurface, the horn antenna is placed at a certain distance during the experiment, so that the spherical wave can be transformed into a plane wave. The minimum distance for antenna placement is shown in the following formula[69] as

$$L_{\min}=2D^2/\lambda\ ,$$

where D is the maximum transverse size of the antenna port (the maximum transverse size of the antenna horn aperture during the experimental test is 13 cm). The frequency of the incident electromagnetic wave is of 8 GHz, the wavelength is of 37.5 mm, and the shortest distance obtained is of 0.9 m. Therefore, the horn antenna should be placed at 0.9 m away from the metasurface, which can meet the requirements of spherical wave to plane wave. During the experiment, the horn antenna was placed at 1.5 m away from the metasurface. The stepper motor

drives the waveguide probe to move for spatial scanning, and the stepper of the motor is of about 10 mm. The transverse sampling number is of 40, and the longitudinal number is of 20. Each step of the motor will stay for a period of time, waiting for the computer to further receive and process the received data, and will return to the starting point after the test. The waveguide probe receives the transmitted wave signal on the test surface. The computer program automatically acquires and processes the received test data for subsequent data integration processing.

Using the experimental test platform, we tested the

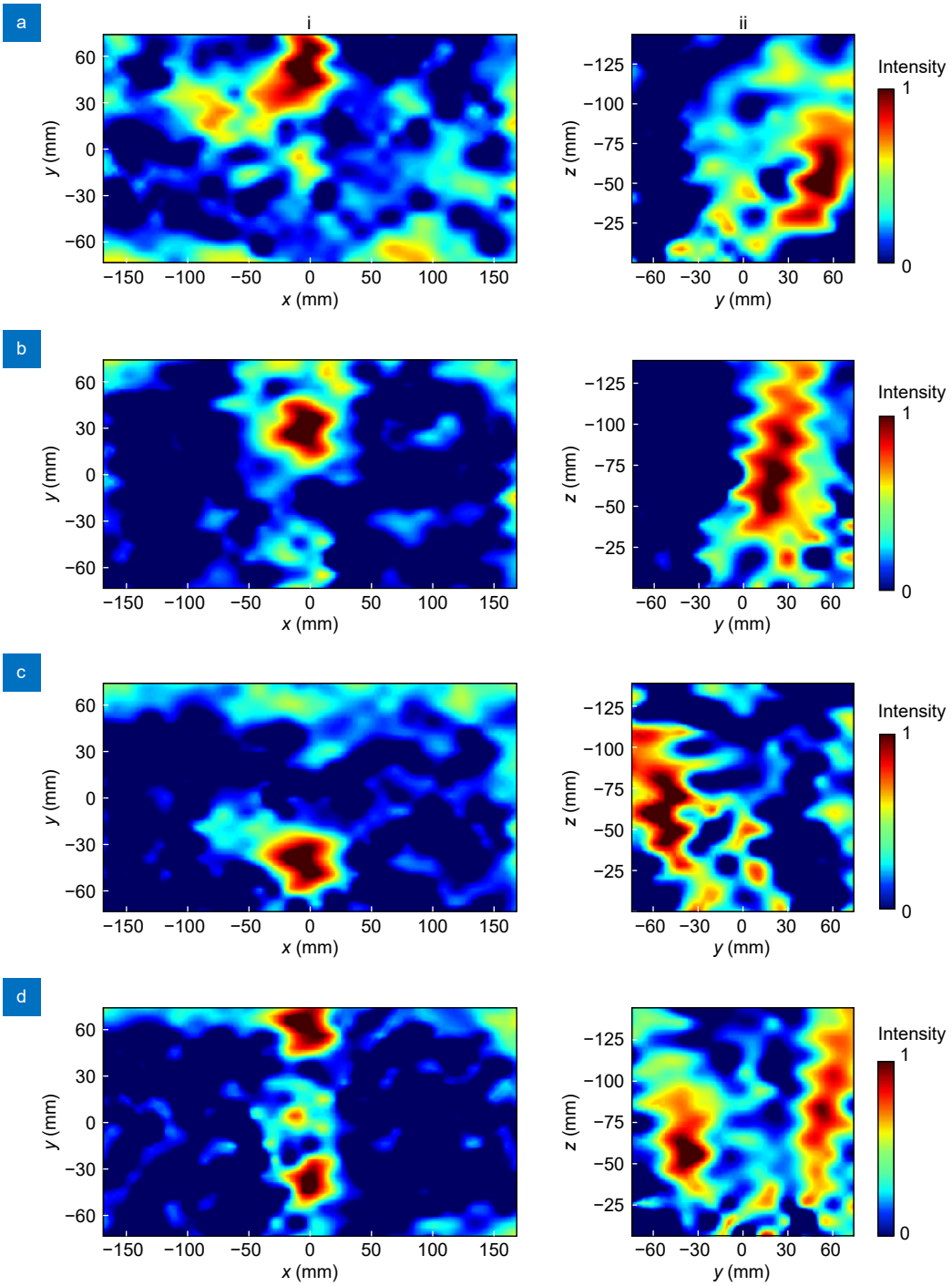

Fig. 13 | The experimental test of the metasurface on the *x*-*y* plane (i) and *y*-*z* plane (ii) in the normal incidence. (**a**) The light intensity distribution of metasurface focusing effect after S2 sequence convolution. (**b**) The light intensity distribution of metasurface focusing effect after S3 sequence convolution. (**c**) The light intensity distribution of the metasurface focusing effect after mixed encoding of the encoding sequence S3 and the reverse encoding sequence S1. (**d**) The light intensity distribution of multi-focus metasurface realized using the additive principle.

focusing function of each metasurface sample, and tested the light intensity distribution of the metasurface on the *x*-*y* plane and *y*-*z* plane, respectively. The focusing effect is shown in Fig.13. It can be observed that each metasurface sample produces a good focusing effect. The metasurfaces for the coding sequence S3 (32*p* period), coding sequence S2 (16*p* period) and mixed coding (coding sequence S3 and reverse coding sequence S1) produce the desired deflection in the y direction. A digitally encoded metasurface lens designed using the additive principle creates two focusing points. But in Fig. 13, the left images appear to be noisy, and the focusing patterns in the right images appear to be jagged, this is because the experimental test platform is not completely carried out in the microwave darkroom, but the absorption cotton is used to reduce the influence of clutter on the experimental results. However, it can not completely absorb clutter, so it has a certain impact on the experimental results and produces noise, and the stability of the experimental platform is not good, the stepper motor is used to move the waveguide probe to receive data, and the waveguide probe will produce a certain small amplitude of jitter in the process of movement, resulting in the test result of the zigzag focusing effect as shown in Fig. 13 and Fig. 14. We further verify the focusing effect of electromagnetic waves incident obliquely on the digitally encoded metalens. In the process of experimental testing, the source position is kept unchanged, and the angle between the metasurface sample and the incident light source is controlled. When the electromagnetic wave emitted by the source is incident on the metasurface, the equivalent plane wave is obliquely incident on the metasurface. The horn antenna was aligned with the metasurface at an incident angle of 30° and then the experimental test was performed to obtain the focusing effect as shown in Fig. 14. The focusing points of each metasurface are shifted by the same distance in the same direction. Compared with the focusing effect produced at normal incidence, there is no obvious intensity change, and it is basically consistent with the simulation results. By comparing the simulation results with the data obtained from the experimental tests, it can be confirmed that the wide-angle metalens designed using the digital coding principle can flexibly control the focuses in two-dimensional space and achieve multi-focus focusing.

Conclusion

We propose a supersymmetric lens based on the principle of quadratic phase gradient transformation. The metalens with wide angle focusing can realize focus control in two-dimensional space. We further introduce the Fourier convolution operation encoding metasurface to

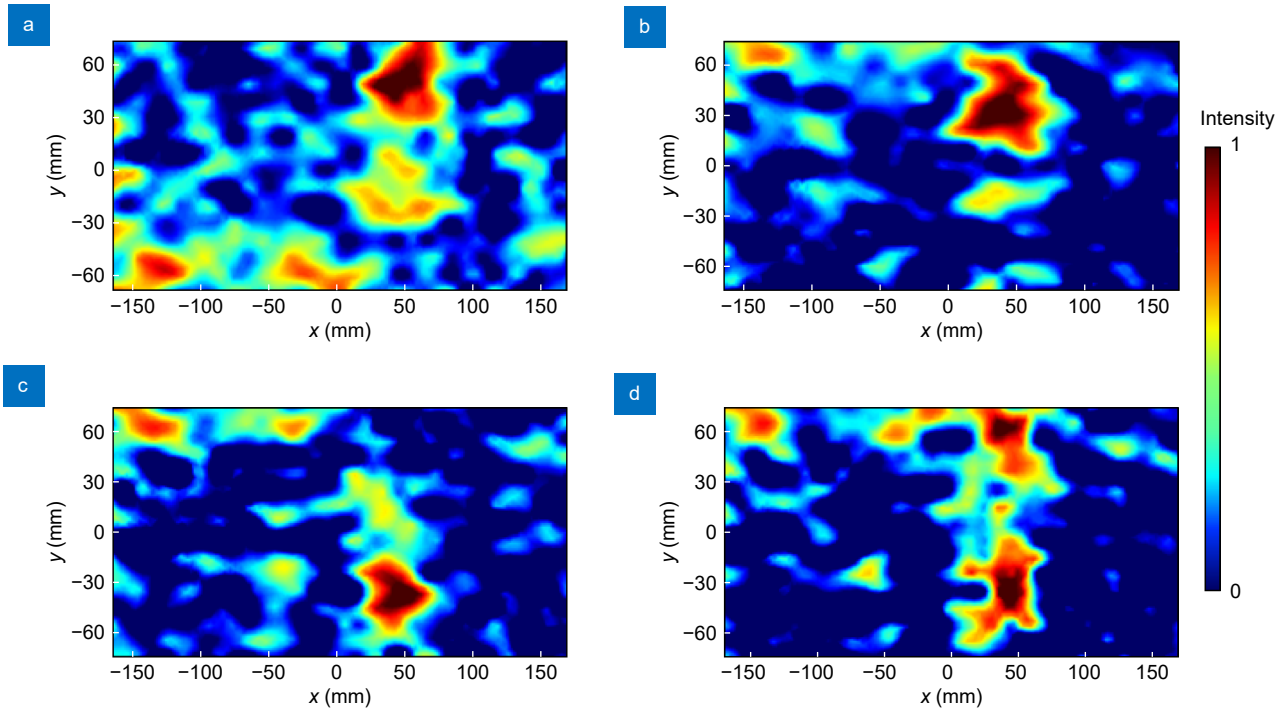

Fig. 14 | The focusing effect of the metasurface in the 30° oblique incidence. (**a**–**d**) are the focused light intensity distribution on the *x*-*y* plane of the four metasurface samples, respectively.

regulate the focal point of the lens in the plane space. Based on the coding addition operation of coding metalens, we can obtain the free control of multi-focus. In the microwave band, we have experimentally confirmed the focus regulation characteristics of the metalens. The theoretical results are basically consistent with the experimental results.

References

1. Zahra S, Ma L, Wang WJ et al. Electromagnetic metasurfaces and reconfigurable metasurfaces: a review. *Front Phys* **8**, 593411 (2021).
2. Hu J, Bandyopadhyay S, Liu YH et al. A review on metasurface: from principle to smart metadevices. *Front Phys* **8**, 586087 (2021).
3. Liu BY, Ren B, Zhao JJ et al. Experimental realization of all-angle negative refraction in acoustic gradient metasurface. *Appl Phys Lett* **111**, 221602 (2017).
4. Panov AV. Possibility of negative refraction for visible light in disordered all-dielectric resonant high index metasurfaces. *Optik* **206**, 163739 (2020).
5. Zhang Y, Yang L, Li XK et al. Dual functionality of a single-layer metasurface: polarization rotator and polarizer. *J Opt* **22**, 035101 (2020).
6. Pfeiffer C, Zhang C, Ray V et al. Polarization rotation with ultra-thin bianisotropic metasurfaces. *Optica* **3**, 427–432 (2016).
7. Yue Z, Li JT, Li J, Zheng CL, Liu JY et al. Terahertz metasurface zone plates with arbitrary polarizations to a fixed polarization conversion. *Opto-Electron Sci* **1**, 210014 (2022).
8. Shen C, Xie YB, Li JF et al. Asymmetric acoustic transmission through near-zero-index and gradient-index metasurfaces. *Appl Phys Lett* **108**, 223502 (2016).
9. Boubakri A, Choubeni F, Vuong TH et al. A near zero refractive index metalens to focus electromagnetic waves with phase compensation metasurface. *Opt Mater* **69**, 432–436 (2017).
10. Badloe T, Kim I, Kim Y et al. Electrically tunable bifocal metalens with diffraction-limited focusing and imaging at visible wavelengths. *Adv Sci* **8**, 2102646 (2021).
11. Zhang YQ, Zeng XY, Ma L et al. Manipulation for superposition of orbital angular momentum states in surface Plasmon polaritons. *Adv Opt Mater* **7**, 1900372 (2019).
12. Yan C, Li X, Pu MB et al. Generation of polarization-sensitive modulated optical vortices with all-dielectric metasurfaces. *ACS Photonics* **6**, 628–633 (2019).
13. Zhu WG, Jiang MJ, Guan HY et al. Tunable spin splitting of Laguerre–Gaussian beams in graphene metamaterials. *Photonics Res* **5**, 684–688 (2017).
14. Zhang XH, Tang DL, Zhou L et al. A quasi-continuous all-dielectric metasurface for broadband and high-efficiency holographic images. *J Phys D Appl Phys* **53**, 465105 (2020).
15. Song QH, Baroni A, Sawant R et al. Ptychography retrieval of fully polarized holograms from geometric-phase metasurfaces. *Nat Commun* **11**, 2651 (2020).
16. Wu Y, Tan SJ, Zhao Y et al. Broadband multispectral compatible absorbers for radar, infrared and visible stealth application. *Prog Mater Sci* **135**, 101088 (2023).
17. Azad AK, Kort-Kamp WJM, Sykora M et al. Metasurface broadband solar absorber. *Sci Rep* **6**, 20347 (2016).
18. Li NX, Fu YH, Dong Y et al. Large-area pixelated metasurface beam deflector on a 12-inch glass wafer for random point generation. *Nanophotonics* **8**, 1855–1861 (2019).
19. Tian Y, Jing XF, Gan HY et al. Free control of far-field scattering angle of transmission terahertz wave using multilayer split-ring resonators' metasurfaces. *Front Phys* **15**, 62502 (2020).
20. Lv HR, Lu XQ, Han YS et al. Multifocal metalens with a controllable intensity ratio. *Opt Lett* **44**, 2518–2521 (2019).
21. Zhang CB, Xue TJ, Zhang J et al. Terahertz meta-biosensor based on high-Q electrical resonance enhanced by the interference of toroidal dipole. *Biosens Bioelectron* **214**, 114493 (2022).
22. Zhang CB, Xue TJ, Zhang J et al. Terahertz toroidal metasurface biosensor for sensitive distinction of lung cancer cells. *Nanophotonics* **11**, 101–109 (2022).
23. Zhang J, Mu N, Liu LH et al. Highly sensitive detection of malignant glioma cells using metamaterial-inspired THz biosensor based on electromagnetically induced transparency. *Biosens Bioelectron* **185**, 113241 (2021).
24. Guan HY, Hong JY, Wang XL et al. Broadband, high-sensitivity graphene photodetector based on ferroelectric polarization of lithium niobate. *Adv Opt Mater* **9**, 2100245 (2021).
25. Li ZH, Liu HP, Zhang XM et al. Metasurface of deflection prism phases for generating non-diffracting optical vortex lattices. *Opt Express* **26**, 28228–28237 (2018).
26. Cheng Y, Cao WH, Wang GQ et al. 3D Dirac semimetal supported thermal tunable terahertz hybrid plasmonic waveguides. *Opt Express* **31**, 17201–17214 (2023).
27. Liu SL, Cao WH, Jiang SZ et al. 3D Dirac semimetal supported tunable multi-frequency terahertz metamaterial absorbers. *Adv Quantum Technol* **7**, 2300386 (2024).
28. Lv HR, Lu XQ, Han YS et al. Metasurface cylindrical vector light generators based on nanometer holes. *New J Phys* **21**, 123047 (2019).
29. Wang H, Liu LX, Zhou CD et al. Vortex beam generation with variable topological charge based on a spiral slit. *Nanophotonics* **8**, 317–324 (2019).
30. Jiang MJ, Zhu WG, Guan HY et al. Giant spin splitting induced by orbital angular momentum in an epsilon-near-zero metamaterial slab. *Opt Lett* **42**, 3259–3262 (2017).
31. Zhang RZ, Guo YH, Li XY et al. Angular superoscillatory metalens empowers single-shot measurement of OAM modes with finer intervals. *Adv Opt Mater* **12**, 2300009 (2024).
32. Li XY, Chen C, Guo YH et al. Monolithic spiral metalens for ultrahigh-capacity and single-shot sorting of full angular momentum state. *Adv Funct Mater* **34**, 2311286 (2024).
33. Zhang S, Li CX, Ke L et al. All-dielectric terahertz wave metagrating lens based on 3D printing low refractive index material. *Infrared Phys Technol* **133**, 104775 (2023).
34. He XY, Lin FT, Liu F et al. 3D Dirac semimetals supported tunable terahertz BIC metamaterials. *Nanophotonics* **11**, 4705–4714 (2022).
35. Lu XQ, Zeng XY, Lv HR et al. Polarization controllable plasmonic focusing based on nanometer holes. *Nanotechnology* **31**, 135201 (2020).
36. Li JT, Li J, Zheng CL et al. Free switch between bound states in the continuum (BIC) and quasi-BIC supported by graphene-metal terahertz metasurfaces. *Carbon* **182**, 506–515 (2021).
37. Li JT, Li J, Zheng CL et al. Dynamic control of reflective chiral terahertz metasurface with a new application developing in full

grayscale near field imaging. *Carbon* **172**, 189–199 (2021).
38. Paniagua-Domínguez R, Yu YF, Khaidarov E et al. A metalens with a near-unity numerical aperture. *Nano Lett* **18**, 2124–2132 (2018).
39. Wang SM, Wu PC, Su VC et al. Broadband achromatic optical metasurface devices. *Nat Commun* **8**, 187 (2017).
40. Gao YF, Gu JQ, Jia RD et al. Polarization independent achromatic meta-lens designed for the terahertz domain. *Front Phys* **8**, 606693 (2020).
41. Pu MB, Li X, Guo YH et al. Nanoapertures with ordered rotations: symmetry transformation and wide-angle flat lensing. *Opt Express* **25**, 31471–31477 (2017).
42. Guo YH, Ma XL, Pu MB et al. High-efficiency and wide-angle beam steering based on catenary optical fields in ultrathin metalens. *Adv Opt Mater* **6**, 1800592 (2018).
43. Zhang F, Pu MB, Li X et al. Extreme-angle silicon infrared optics enabled by streamlined surfaces. *Adv Mater* **33**, 2008157 (2021).
44. Guo YH, Zhang ZJ, Pu MB et al. Spoof plasmonic metasurfaces with catenary dispersion for two-dimensional wide-angle focusing and imaging. *iScience* **21**, 145–156 (2019).
45. Guo YH, Zhang SC, Pu MB et al. Spin-decoupled metasurface for simultaneous detection of spin and orbital angular momenta via momentum transformation. *Light Sci Appl* **10**, 63 (2021).
46. Zhang F, Guo YH, Pu MB et al. Meta-optics empowered vector visual cryptography for high security and rapid decryption. *Nat Commun* **14**, 1946 (2023).
47. Liu S, Cui TJ, Zhang L et al. Convolution operations on coding metasurface to reach flexible and continuous controls of terahertz beams. *Adv Sci* **3**, 1600156 (2016).
48. Yu NF, Genevet P, Kats MA et al. Light propagation with phase discontinuities: generalized laws of reflection and refraction. *Science* **334**, 333–337 (2011).
49. Wu RY, Shi CB, Liu S et al. Addition theorem for digital coding metamaterials. *Adv Opt Mater* **6**, 1701236 (2018).
50. Ha YL, Luo Y, Pu MB et al. Physics-data-driven intelligent optimization for large-aperture metalenses. *Opto-Electron Adv* **6**, 230133 (2023).
51. Kan YH, Bozhevolnyi SI, Kumar S. Large spontaneous emission enhancement with silver nanocube dimers on silver substrates. *Adv Quantum Technol* **6**, 2300196 (2023).
52. Chen J, Wang DP, Si GY et al. Planar peristrophic multiplexing metasurfaces. *Opto-Electron Adv* **6**, 220141 (2023).
53. Howard S, Esslinger J, Wang RHW et al. Hyperspectral compressive wavefront sensing. *High Power Laser Sci Eng* **11**, e32 (2023).
54. Achouri K, Tiukuvaara V, Martin OJF. Spatial symmetries in nonlocal multipolar metasurfaces. *Adv Photonics* **5**, 046001 (2023).
55. Liu ZY, Wang DY, Gao H et al. Metasurface-enabled augmented reality display: a review. *Adv Photonics* **5**, 034001 (2023).
56. Cui DZ, Yi XX, Yang LP. Quantum imaging exploiting twisted photon pairs. *Adv Quantum Technol* **6**, 2300037 (2023).
57. Wang GQ, Madonini F, Li BN et al. Fast wide-field quantum sensor based on solid-state spins integrated with a SPAD array. *Adv Quantum Technol* **6**, 2300046 (2023).
58. Huang YJ, Xiao TX, Chen S et al. All-optical controlled-NOT logic gate achieving directional asymmetric transmission based on metasurface doublet. *Opto-Electron Adv* **6**, 220073 (2023).
59. Du WY, Zhu MP, Shi J et al. Effect of subsurface impurity defects on laser damage resistance of beam splitter coatings. *High Power Laser Sci Eng* **11**, e61 (2023).
60. Döpp A, Eberle C, Howard S et al. Data-driven science and machine learning methods in laser–plasma physics. *High Power Laser Sci Eng* **11**, e55 (2023).
61. Khazanov E. Reducing laser beam fluence and intensity fluctuations in symmetric and asymmetric compressors. *High Power Laser Sci Eng* **11**, e93 (2023).
62. Koshelev KL, Tonkaev P, Kivshar YS. Nonlinear chiral metaphotonics: a perspective. *Adv Photonics* **5**, 064001 (2023).
63. Zhao BY, Mertz J. Resolution enhancement with deblurring by pixel reassignment. *Adv Photonics* **5**, 066004 (2023).
64. Li Y, Huang XJ, Liu SX, Liang HW, Ling YY et al. Metasurfaces for near-eye display applications. *Opto-Electron Sci* **2**, 230025 (2023).
65. Gao H, Fan XH, Wang YX et al. Multi-foci metalens for spectra and polarization ellipticity recognition and reconstruction. *Opto-Electron Sci* **2**, 220026 (2023).
66. Xiao YT, Chen LW, Pu MB et al. Improved spatiotemporal resolution of anti-scattering super-resolution label-free microscopy via synthetic wave 3D metalens imaging. *Opto-Electron Sci* **2**, 230037 (2023).
67. Bao B, Hua Y, Wang RD et al. Quantum-based magnetic field sensors for biosensing. *Adv Quantum Technol* **6**, 2200146 (2023).
68. Geller MR. Fast quantum state discrimination with nonlinear positive trace-preserving channels. *Adv Quantum Technol* **6**, 2200156 (2023).
69. Liang Y, Dong YY, Jin YX et al. Terahertz vortex beams generated by the ring-arranged multilayer transmissive metasurfaces. *Infrared Phys Technol* **127**, 104441 (2022).

Acknowledgements

This work was supported in part by the Science and technology innovation leading talent project of special support plan for high-level talents in Zhejiang Province (2021R52032); Natural Science Foundation of Zhejiang Province under grant No. LY22F050001; Special project for professional degree postgraduates of Zhejiang Provincial Education Department (No.Y202353663; Y202353686), and in part by the National Natural Science Foundation of China under grant No. 62175224. China Jiliang University Basic Research Expenses.

Competing interests

The authors declare no competing financial interests.

Scan for Article PDF